FEASIBILITY AND PERFORMANCE ANALYSIS OF MAGNETOHYDRODYNAMIC CONTROL FOR AEROCAPTURE AT NEPTUNE

Danny N. Nguyen,[*] Soumyo Dutta,[†] Robert W. Moses,[‡] Hisham K. Ali,[§] and Brian C. Gunter [**]

NASA's most recent Decadal Survey posed a mission to one of the Ice Giants as the top priority for flagship missions in the organization's future. However, current technologies limit the amount of scientific payload available for future Uranian and Neptunian missions due to the need for fuel for orbit insertion maneuvers. Thus, to maximize the scientific potential of future missions, atmospheric aerocapture has been heavily researched. While atmospheric aerocapture simulations have proven enabling for capturing around Neptune, its deep atmospheric pass requires an aeroshell with thermal protection systems (TPS). Magnetohydrodynamically-controlled aerocapture serves as a potential solution to both fully-propulsive orbit insertion and atmospheric aerocapture. Through NASA Langley's high-fidelity flight dynamics simulation, the Program to Optimize Simulated Trajectories II, both the atmospheric and magnetohydrodynamic aerocapture methods were simulated and compared for identical missions to Neptune. After applying a guidance algorithm for both methods, the results showed that magnetohydrodynamics has not only the control authority to successfully capture around Neptune, but also the unique advantage of a shallower atmospheric pass which decreases the maximum heat load and the required TPS mass.

INTRODUCTION

While spacecraft have successfully made it to the surface of Mars and into a flyby of the outer planets, the technologies from these missions are reaching the threshold of their capabilities. These traditional methods are inadequate for higher mass and outer planetary missions due to the inherent propellant mass constraints of using fully propulsive orbital insertion. Thus, there has been an ongoing effort to introduce new methods of deceleration and flight control during planetary entry,

---

[*] Graduate Research Assistant, Ann & H.J. Smead Department of Aerospace Engineering Sciences, University of Colorado Boulder, Boulder, CO 80303, USA.

[†] Aerospace Engineer, Atmospheric Flight and Entry Systems Branch, NASA Langley Research Center, Hampton, VA 23666, USA.

[‡] Independent Contractor, Formerly from NASA Langley Research Center, Hampton, VA 23666, USA.

[§] Assistant Professor, Ann & H.J. Smead Department of Aerospace Engineering Sciences, University of Colorado Boulder, Boulder, CO 80303, USA.

[**] Associate Professor, Daniel Guggenheim School of Aerospace Engineering, Georgia Institute of Technology, Atlanta, GA 30313, USA.

descent, and landing to reduce the required propellant mass and enable new missions. One of the most prominently proposed solutions is atmospheric aerocapture.[1, 2, 3, 4, 5, 6, 7, 8]

Aerocapture is the use of a planet's atmosphere to maneuver a spacecraft and capture into an orbit around that planet. As shown in Figure 1, during aerocapture, the spacecraft will enter hyperbolically into the atmosphere, begin its guidance to be put onto a trajectory towards some target parking orbit, and then finally perform a few corrective maneuvers to adjust for any inevitable uncertainties or perturbations. While these corrective maneuvers will require propulsive burns, these burns will be considerably less than the burns that would have been required if aerocapture had not been applied. It is the goal of the controlled guidance during the atmospheric phase of the flight to minimize the required propellant for these corrective maneuvers while attaining the desired orbit. With successful guidance and control, propellant mass for orbital insertion can be significantly reduced, and that mass can then be used for scientific payload to enable larger missions to farther targets such as Uranus and Neptune.
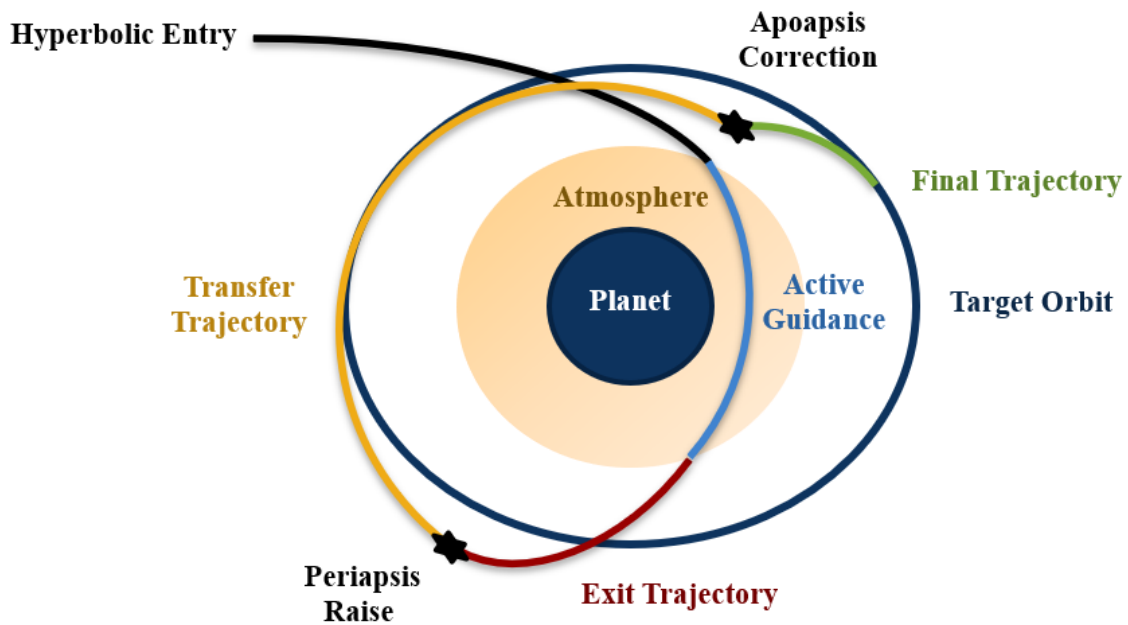

Fig 1. Aerocapture Concept of Operations.

In traditional aerodynamic aerocapture, the guidance is performed in one of three ways: direct force control (DFC), bank angle modulation (BAM), or drag control. The primary methods considered in this report are only DFC and BAM since these are controlled solely with the vehicle's aerodynamic angles. DFC actively adjusts the angles of attack and sideslip to directly manipulate the lift and drag vectors and forces to shape the spacecraft trajectory. BAM actively adjusts the bank angle to roll the spacecraft and indirectly change the direction of the vehicle lift force. While research studies have proven considerable reductions in propellant mass with the use of both DFC and BAM,[6,9] relying on the atmospheric density and the resulting aerodynamic forces poses a few disadvantages.

Specifically, the thermal protection system (TPS) on the spacecraft must be more robust in order to survive the pass. Thus, although saving propellant mass, atmospheric aerocapture must add

considerable TPS mass in return. Although these propellant savings typically still outweigh this additional TPS mass,[9,10] an alternative which minimizes both the propellant mass and the TPS mass would be the ideal solution to begin enabling these previously infeasible missions.

This research proposes magnetohydrodynamic (MHD) control as that solution. MHD control takes advantage of the electrically conductive, ionized plasma that is created during the spacecraft's hypersonic entry into a planet's atmosphere. By introducing a controllable magnetic field through onboard electromagnets to the surrounding conductive plasma, Lorentz forces can be created and applied onto the spacecraft. These induced Lorentz forces can then supplement or even replace aerodynamic forces as a control method in aerocapture. In fact, solely MHD-controlled aerocapture is theorized to have a unique advantage over its traditional atmospherically controlled counterpart because of its ability to be activated much higher in the atmosphere while still achieving the same magnitudes of force and control authority.[11] Thus, MHD-controlled aerocapture has the potential to not only achieve propellant mass reductions on par with that of its atmospheric counterpart but also minimize TPS mass.

METHODOLOGY

Physical Design of Magnetohydrodynamic Control

This study serves to prove MHD-controlled aerocapture can improve upon its atmospheric predecessor. The aerodynamic angle modulations required for both DFC and BAM can be controlled through either an internal ballast which applies a torque about the spacecraft's center of gravity or an external aerodynamic control surface, such as a flap, to tilt and rotate the spacecraft. On the other hand, magnetohydrodynamics would be applied using a permanent magnet or an electromagnet; in this study, a configuration of two electromagnets is used to allow for controllability. By using two static electromagnets stationed in the body's x- and z-axes, as shown in Figure 2,[*] the induced Lorentz force can be magnified and even directed by simply changing the current to each electromagnet. For example, forcing the current solely into the z-axis-stationed electromagnet will maximize the magnetic pitch angle and the z-component of the magnetic field, which directly increases the induced drag.
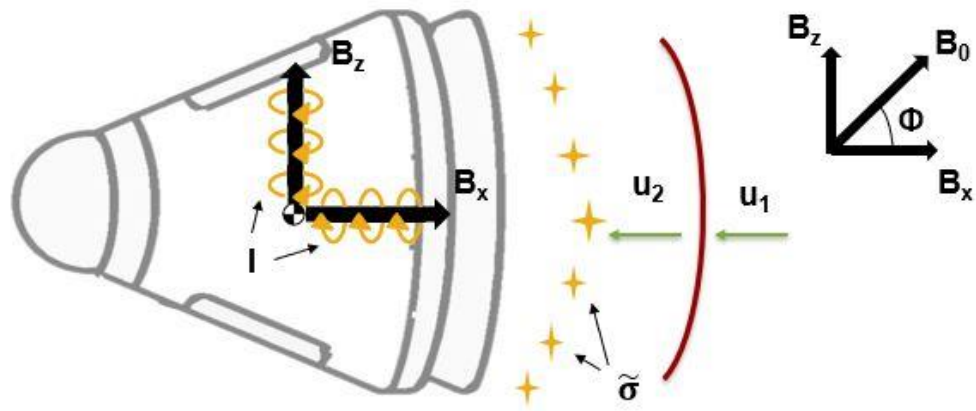
Fig. 2 Electromagnet Configuration for MHD-Controlled Aerocapture

An important note to make about this configuration is that both electromagnets are configured at the spacecraft's center of gravity. This ensures ballistic entry and prevents the spacecraft from rotating and producing any incidental aerodynamic angles and forces. This is preferred for the purposes of this research because it ensures that the control and subsequent aerocapture are solely due to magnetohydrodynamic control and not due to any additional aerodynamic forces if the spacecraft rotates. There is an argument towards placing the configuration closer to the ionized plasma at the surface of the spacecraft to allow for higher control authority; however, since this research serves as only a proof of concept of MHD-controlled aerocapture, uncoupling the MHD control allows for a clearer understanding of its effect.

The preliminary design for each electromagnet in this configuration focused on minimizing the electromagnet's mass, m, and required power, P, while still achieving a functional magnetic field strength, B_0, and fusing time, where the fusing time, t_{fuse}, is defined as the amount of time the maximum current, I, could be applied before the electromagnet's wires melt. The mass, power, and magnetic field strength are defined through Eqs. (1) through (4) below. Lastly, the electrical fusing time is defined through Onderdonk's equation shown in Eq. (5) where the initial wire temperature, T_{init}, is set to be roughly room temperature. This serves as a conservative preliminary estimate of the fusing time since the initial temperature will change and will likely be lower than room temperature in actual applications.

$$m = A_w l_w \rho_w \tag{1}$$

$$l_w = 2\pi r_c N \tag{2}$$

$$P = \frac{4\pi r_c^2}{\mu_0 A_w \sigma_w} * B_0 I \tag{3}$$

$$B_0 = \frac{N\mu_0}{2r_c} * I \tag{4}$$

$$t_{fuse} = 1.15 * 10^5 \log_{10}\left(\frac{T_{melt} - T_{init}}{233 + T_{init}} + 1\right)\left(\frac{A_w}{I}\right)^2 \tag{5}$$

As seen in the equations above, the mass and power constraints are heavily dependent on the wire's area, A_w, length, l_w, mass density, ρ_w, and conductivity, σ_w. Thus, the wire material and size serve a significant role in MHD performance. The most common materials used for electromagnetic coil wires are copper and aluminum. While copper is more electrically conductive, it is also denser; thus, the material choice becomes a tradeoff between power and mass. On top of that, the melting point of copper is higher than that of aluminum which inherently allows the copper to last longer against fusing concerns. If only the wire materials are varied, the options are is shown in Table 1. While aluminum requires more power and has a shorter fusing time than copper, its mass difference significantly outweighs the disadvantages in power and fusing time. Thus, aluminum was chosen as the electromagnet material type moving forward.

Table 1. Wire Material Trade Study.

	Copper	Aluminum	Percent Difference, %
Mass (kg)	119.80	36.23	107.11
Power (W)	21,460.71	33,851.72	44.80
Electrical Fusing Time (s)	862.80	659.47	26.71

With the material decided, the electromagnet design becomes a multivariable optimization problem, minimizing the mass and power while maximizing the magnetic field strength and fusing time. The variables which directly affect this optimization are the electromagnetic current, coil radius, cross-sectional wire area, and the number of turns. These four variables were altered until a reasonable mass, power, magnetic field strength, and fusing time were all achieved. For the purposes of this research, the preliminary point design for a single electromagnet defined in Table 2 will suffice; however, future research efforts may perform more robust optimization to achieve an ideal electromagnet design.

There are two important notes to make on Table 2. First, the constraints are calculated under the conservative assumption that the maximum current will be applied continuously. In reality, the current will vary between zero and the maximum value as necessary, which would give the power and fusing time some flexibility from these values. Secondly, the design defined is only for a single electromagnet and not the electromagnet configuration. Thus, for the full configuration, the mass and required power values would be twice the listed values while all the other variables would remain the same.

Table 2. Electromagnet Point Design.

Design Parameter	Value
Max Current (A)	130
Coil Radius (m)	0.10
Wire Gauge (AWG)	6
Number of Turns	1,600
Mass (kg)	36.23
Max Required Power (W)	33,851.72
Max Magnetic Field Strength (T)	1.508
Minimum Fusing Time (s)	659.5

Although the power required may seem daunting, this power can be created through magnetohydrodynamic power generation. Previous research has shown MHD power generation to

create usable power on the order of hundreds or even thousands of kilowatts.[12,13] In this case, assuming an ideal Faraday MHD generator, the maximum power per unit volume that MHD can generate at any given time is roughly estimated through Equation (6), where $\tilde{\sigma}$ and u_2 are the effective electrical conductivity and post-shock local velocity, respectively.[12] As seen in Figure (3), the power generated with a MHD generator with even a thousandth of the volume of each electromagnet can produce upwards of 16,000 kW of power. Figure (3) also shows the bounds at which the power produced becomes sufficient to power both electromagnets. Thus, within these bounds, MHD control is entirely self-powering. Future research may work to widen these bounds; however, for the purposes of this research, the volume and subsequent mass of the generator were made to be relatively negligible.

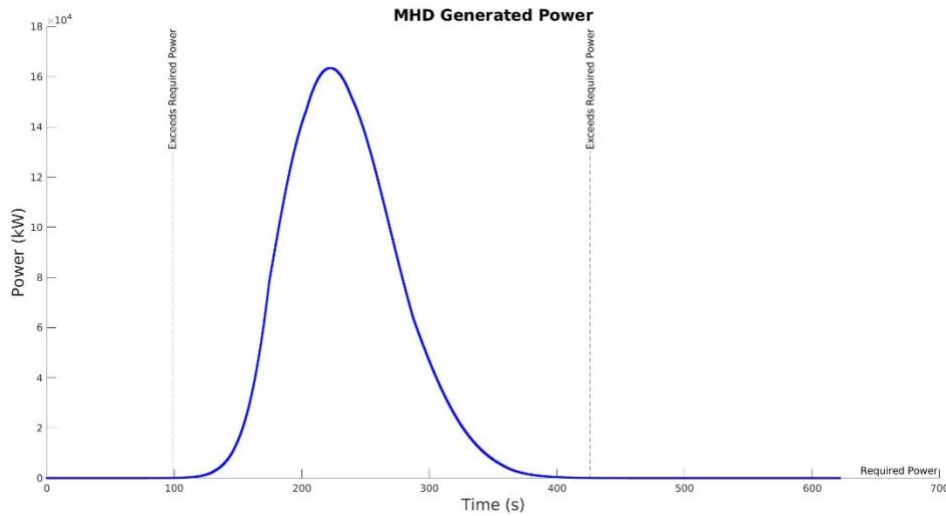$$P_{MHD} = \frac{1}{4} * \tilde{\sigma} * u_2^2 * B_0^2 \tag{5}$$

Figure 3. MHD generated power.

Another unique constraint of MHD control is the fusing time of the electrical wire. While DFC and BAM do not have a limit on their guidance time, MHD control must capture before the wires of the electromagnet melt. The results from DFC and BAM simulations performed later in this study have found the guidance to last typically under 600 seconds. Thus, if magnetohydrodynamics can perform on par with its atmospheric counterparts, the designed fusing time should be sufficient for MHD control.

Finally, the additional mass due to the electromagnets must be considered as well. Based on previous research using atmospheric aerocapture for trajectories to Neptune, the required thermal protection system mass to support the atmospheric pass was roughly 556.6 kilograms.[3] It is important to note that the referenced mass is for a mid-L/D vehicle whereas the vehicle in this study is a blunt body; therefore, the mass serves more as an estimate of the TPS mass rather than a direct comparison. Despite this caveat, it is evident that the additional mass from the electromagnetic configuration is a relatively small fraction of the TPS mass typically required for atmospherically

controlled aerocapture. Thus, if the TPS mass savings from using MHD control can exceed this additional electromagnet mass, then MHD-controlled aerocapture may prove to be advantageous.

Simulation Models for Atmospheric and Magnetohydrodynamic Aerocapture

To allow for a direct comparison between MHD-controlled aerocapture and atmospherically controlled aerocapture, the simulations were made as identical as possible with the only difference being the control method. These trajectory simulations were both created in NASA Langley's Program to Optimize Simulated Trajectories II (POST2).[14] This program allowed for precise trajectory integration and optimization while using robust spacecraft aerodynamic and aeroheating models as well as planetary gravitational and atmospheric models. The aerodynamic model is specified for a 70-degree sphere-cone reentry forebody whereas the aeroheating is calculated by the Sutton-Graves model with specific inputs for Neptune. Neptune was chosen as the target of interest not only because of its large need for mission-enabling mass savings but also because of its relatively dense atmosphere when compared to other gas giants. These vehicle and planetary models used are predefined options built into POST2 which have years of history and extensive uses throughout several NASA missions and research efforts.[8,15]

Table 3. Vehicular and Planetary Models.

	Model
Aerodynamic Model	MSL Aerodatabase[16,17]
Aeroheating Model	Sutton-Graves, Cold-Wall Convective Indicator
Gravitational Model	Unnormalized Oblate Planet Model up to J2
Atmospheric Model	2004 Neptune GRAM[18,19]

While these shared models define all the necessary factors playing a role in atmospheric aerocapture and several of the key components in MHD controlled aerocapture, MHD control cannot be modeled without two crucial additions: the electrical conductivity model and the MHD induced Lorentz force model. The electrical conductivity, σ, is modeled as a piecewise function of three variables: the gas number density, n, the electron number density, n_e, and the electron temperature, T_e, as seen in Equation (7). Through the Langley Aerothermodynamic Upwind Relaxation Algorithm (LAURA),[20] a computational fluid dynamics simulation software code, these variables were calculated with confidence for velocities between 16 and 32 km/s and for atmospheric densities between 10^{-6} to 10^{-3} kg/m^3. While this velocity range is representative of the stages of aerocapture, these densities are not comprehensive of all the altitudes MHD control can operate at. However, expanding the range of densities below 10^{-6} kg/m^3 requires a more complex direct simulation Monte Carlo solver instead of the currently used Navier-Stokes solver because of the rarefied flow below that density. Thus, values below 10^{-6} kg/m^3 were estimated through logarithmic extrapolation until 10^{-10} kg/m^3 where any further values were considered negligible.

$$\sigma = \begin{cases} 3 * 10^5 \left(\dfrac{n_e}{n}\right), & \dfrac{n_e}{n} \leq 10^{-3} \\ 2.147 * 10^{-3} (T_e)^{\frac{3}{2}}, & \dfrac{n_e}{n} > 10^{-3} \end{cases} \tag{7}$$

With the variables of interest defined, the piecewise electrical conductivity function can be separated into two parts based on the ionization fraction, or the ratio of the electron number density to the gas number density. Below the ionization fraction threshold, electrical conductivity is only a function of the ionization fraction; however, above the ionization fraction threshold, electrical conductivity becomes dependent on only the electron temperature. The ionization fraction and electron temperature for this specific trajectory are shown in Figures (4) and (5) below. Figure (4) shows that the ionization fraction is always above the threshold; therefore, only the electron temperature dependent equation is used. Since MHD control begins in the rarefied regime, Figure (5) depicts the electron temperature with both the precise data from LAURA as well as the logarithmic extrapolation when densities dip below the threshold for the provided look up table, as shown in Figure (6).
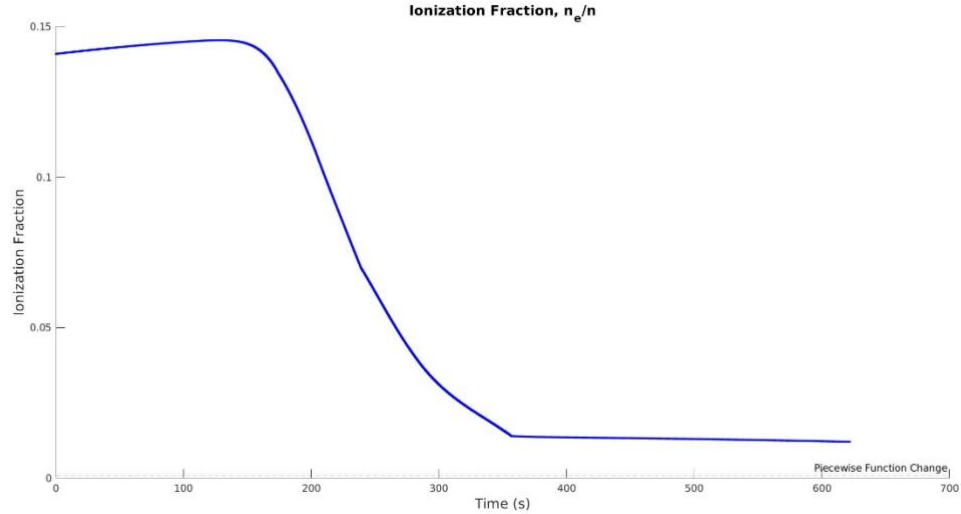

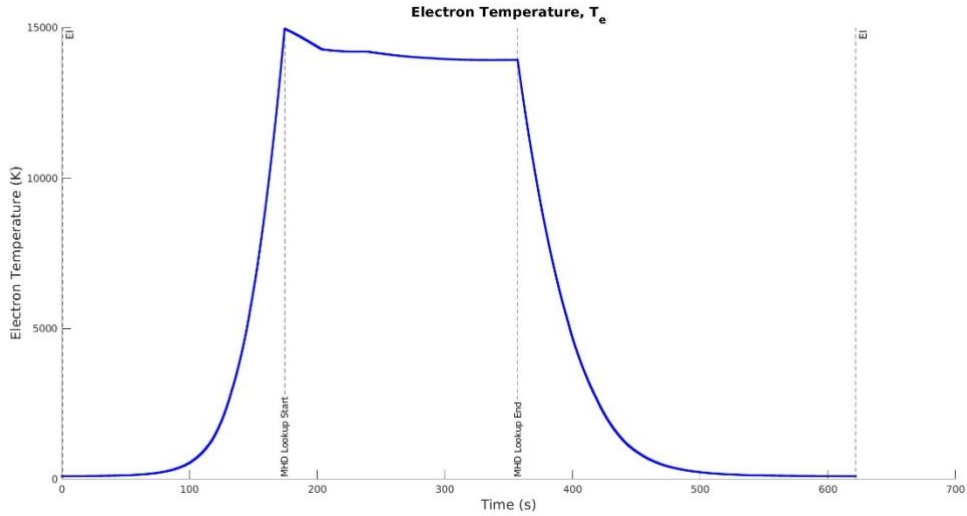**Figure 4. Ionization fraction during atmospheric entry.**

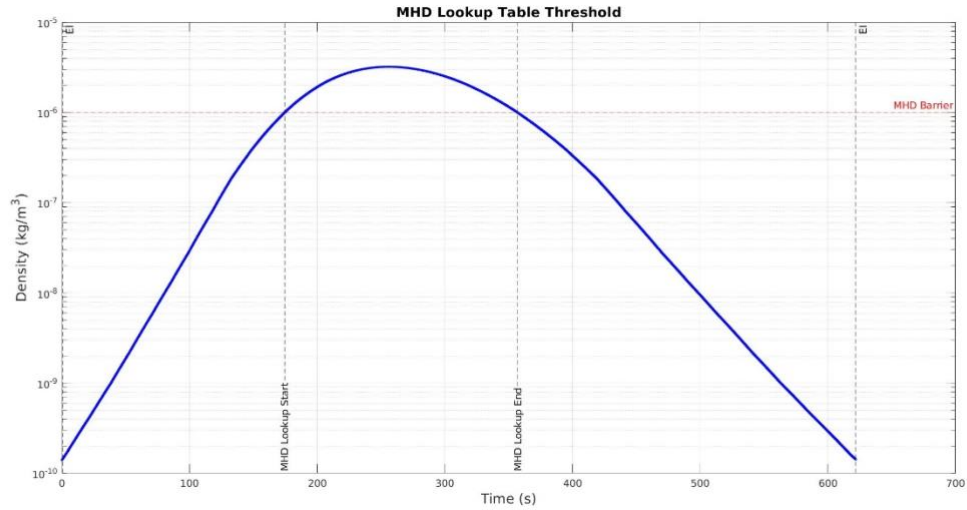**Figure 5. Electron temperature during atmospheric entry.**

Figure 6. Atmospheric density threshold for LAURA data.

Although LAURA shows that the electrical conductivity and MHD control authority increases with velocity, the electron and ion mobility are inversely proportional with velocity. Thus, with larger velocities, the ions and electrons begin to slow down against the bulk neutral gas causing ion slip, which reduces the effectiveness of MHD control. Ion mobility, μ_i, and electron mobility, μ_e, are defined in Equations (8) and (9), where n_n, n_i, m_i, and T_2 are the neutral species number density, ion number density, ion particle mass, and post-shock atmospheric velocity, respectively. For the purposes of this research, the ion number density is assumed to be equal to the electron number density since LAURA assumes a neutral plasma. Furthermore, the ion particle mass is calculated using the mean molecular weight of the Neptunian atmosphere. Lastly, the Coulomb logarithm, $\ln(\Lambda)$, is the factor of dominance between small-

angle collisions and large-angle collisions. This term is a property of the plasma and can typically be set as a constant value between 10 and 20.[21] In this case, a mean value of 15 was chosen. Finally, the electrical conductivity can be adjusted for ion slip using Eq. (10). As seen in Figure (7), while introducing ion slip reduces the electrical conductivity, it also normalizes the curve and makes the electrical conductivity behave more realistically.

$$\mu_i = \frac{1}{2} * \frac{2}{(n_n^{-1} * 2.2 * 10^{10} * (m_i * T_2)^{-0.5})^{-1} + (14.3 * m_i^{-0.5} * T_2^{1.5} * n_i^{-1})^{-1}} \tag{8}$$

$$\mu_e = \frac{1}{2} * \frac{2}{\left(n_n^{-1} * 3.74 * 10^{19} * e^{33.5*(\ln(T_e))^{-0.5}}\right)^{-1} + (n_i^{-1} * 9.5 * 10^{16} * T_e^{1.5} * \ln(\Lambda)^{-1})^{-1}} \tag{9}$$

$$\tilde{\sigma} = \frac{\sigma}{1 + \mu_i * \mu_e * \left|\overrightarrow{B_0}\right|^2} \tag{10}$$
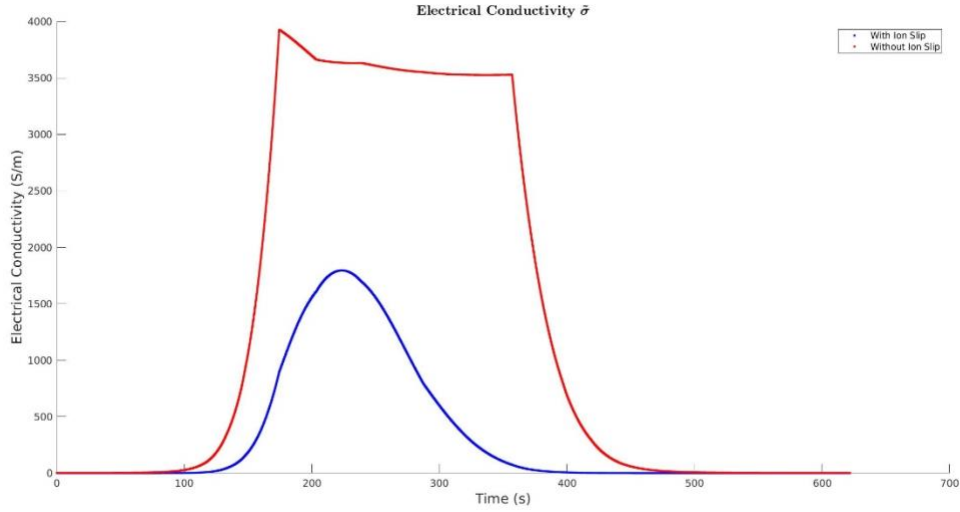

Figure 7. Electrical conductivity before and after ion slip correction.

With the effective electrical conductivity, $\tilde{\sigma}$, model defined, the magnetohydrodynamically-induced Lorentz force can be calculated and combined into the POST2 trajectory integration. Because of the ideal atmospheric conditions of Neptune with regards to MHD, the Hall effect can be deemed negligible, and thus, the induced Lorentz side force can also be ignored.[15] This leaves the induced forces on the body x- and z-axes which are calculated through Eqs. (11) through (15) below, where K, u_2, and A_{patch} are the load factor, post-shock velocity, and MHD patch area, respectively. The load factor is a constant defined by the relationship between the load resistance and the plasma resistance. This is a value between zero and one, and for the purposes of this research, a mean value of 0.5 was chosen.

$$F_x = -(1 - K)\tilde{\sigma}u_2 B_z^2 A_{patch} \tag{11}$$

11

$$F_z = (1 - K)\tilde{\sigma}u_2 B_z B_x A_{patch} \tag{12}$$

$$B_x = B_0 \cos(\phi) \tag{13}$$

$$B_z = B_0 \sin(\phi) \tag{14}$$

$$A_{patch} = \pi r_c^2 \tag{15}$$

This study concentrated on an open-loop implementation of MHD-based guidance for aerocapture where the MHD force is kept constant. To simplify the targeting and optimization problem, the magnetic field vector magnitude is kept at a constant value so that the MHD pitch angle, Φ, is the only controllable independent variable. This essentially forces the electromagnet configuration's total electric current to remain constant. Thus, decreasing the current to one electromagnet will increase the current to the other electromagnet to equally. In reality, this would be impractical, and the total current would decrease to conserve power as needed. However, because of the excess power available through MHD power generation,[12,13] this simplification is feasible for the purposes of this research. After applying all of these equations, these MHD-induced Lorentz forces were then integrated into the total force calculation to allow the vehicle to move and react to the additional forces accordingly.

Guidance Algorithms for Atmospheric and Magnetohydrodynamic Aerocapture

After modeling the underlying physics of atmospheric and magnetohydrodynamic control, the guidance algorithm behind each control method was developed. For this research to Neptune, the guidance aimed to capture into a target orbit which allowed for Triton flybys, maximizing the potential scientific benefit of this mission. The orbital parameters of this target orbit are given in Table 4 below.

Table 4. Target Orbit Characteristics.

Target Orbital Parameter	Value
Apoapsis Altitude (km)	430,000
Periapsis Altitude (km)	3,986
Longitude of the Ascending Node (º)	330.829
Inclination (º)	153.547

Aerodynamic aerocapture uses a robust numerical predictor-corrector algorithm to perform closed-loop guidance and optimize the aerodynamic angle as necessary. The algorithm used is Fully Numerical Predictor-corrector Aerocapture Guidance algorithm (FNPAG). FNPAG is a well-established and supported algorithm which can actively optimize multiple variables at once while targeting some given variable.[22,23] For the direct force control case, the angle of attack and the side slip angles were actively optimized to target a mean apoapsis altitude of 430,000 km. Similarly, for the bank angle modulation case, the bank angle was actively optimized to target the same mean apoapsis altitude.

On the other hand, the MHD controlled aerocapture simulation utilizes open-loop guidance instead of the more robust closed loop active guidance applied in its atmospheric counterpart. While closed-loop active guidance with off-nominal Monte Carlo case studies would be ideal and will be done in the follow-up research, this study is the first step in proving the capabilities and advantages of the general, nominal MHD-controlled aerocapture.

As mentioned in the electromagnet configuration design, the electromagnets were placed at the center of gravity. To test just the effect of MHD forces on aerocapture without relying on lift modulation of the aerodynamic forces, there is no radial offset in the center of gravity and the aerodynamic angles and lift-to-drag ratio will be set to zero as well. Using the maximum current configuration defined in Table 2 and an MHD pitch angle of 90°, MHD control successfully captured in roughly 621 seconds. Thus, even with the most power-intensive approach, the spacecraft can capture without passing the fusing time limit. Furthermore, MHD control only required an entry flight path angle of -11.0427° to capture.

On the other hand, the direct force control method required a flight path angle of -12.355° while the bank angle control method required -12.687°. This is an important distinction because a steeper entry flight path angle indicates a deeper pass which requires a more robust and more massive TPS system. Thus, the entry flight path angle has a direct relationship with the additional TPS mass this research aims to minimize. Therefore, with a roughly 1° – 1.5° difference in the flight path angle, we can expect MHD control to have a reduced required TPS mass. These flight path angles, guidance times, and flight trajectories are shown in Table 5 and Figure (9), respectively.

Table 5. Guidance Method Performance.

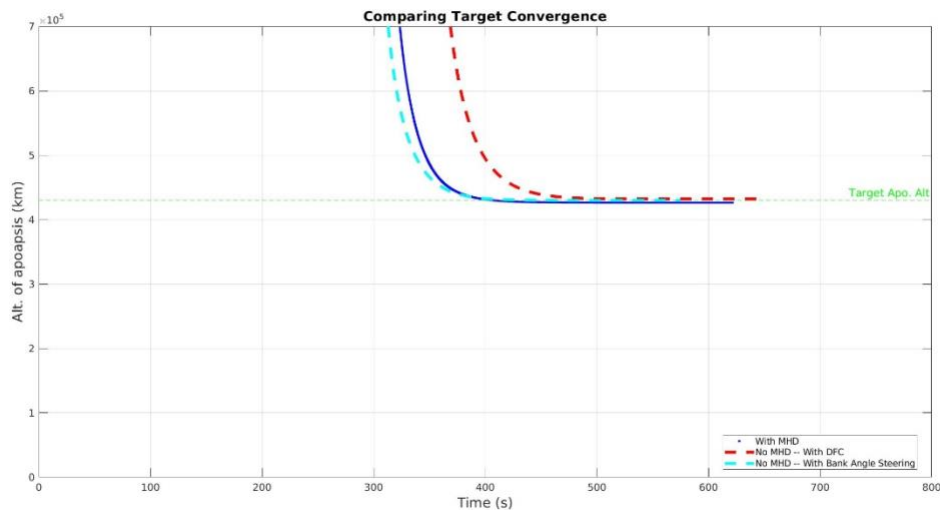|	Direct Force Control	Bank Angle Modulation	MHD Control
Flight Path Angle (°)	-12.3550	-12.6870	-11.0427
Guidance Time (s)	649.3	574.7	585.6

Fig 9. Guidance Method Convergence with Target Orbit

13

RESULTS

Finally, the shallower flight path angle from MHD control should allow the spacecraft to pass through the atmosphere at a much higher altitude. This pass is shown in Fig. (10) where the MHD-controlled pass is almost 100 kilometers higher than the atmospherically controlled passes.

Being able to pass at a significantly higher altitude while still retaining the same control authority is a notable feat because it allows the spacecraft to considerably decrease the heat it experiences as it traverses through the atmosphere. As shown in Figure (11), MHD control is capable of inducing forces on par with those of DFC and BAM control. The forces are depicted as a root sum of squares of all the forces acting on the body x, y, and z axes. The jump shown in the DFC force plot is inherent to the nature of DFC control.
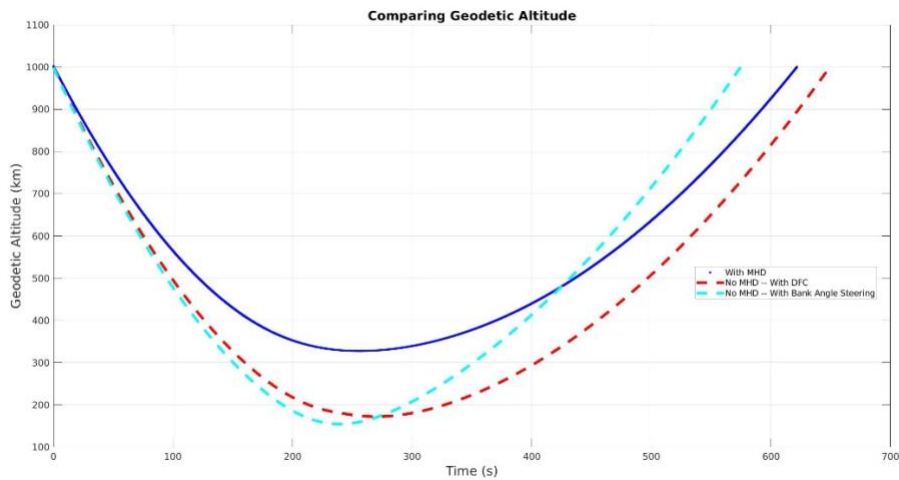
Fig. 10 Geodetic Altitude during each Control Method.
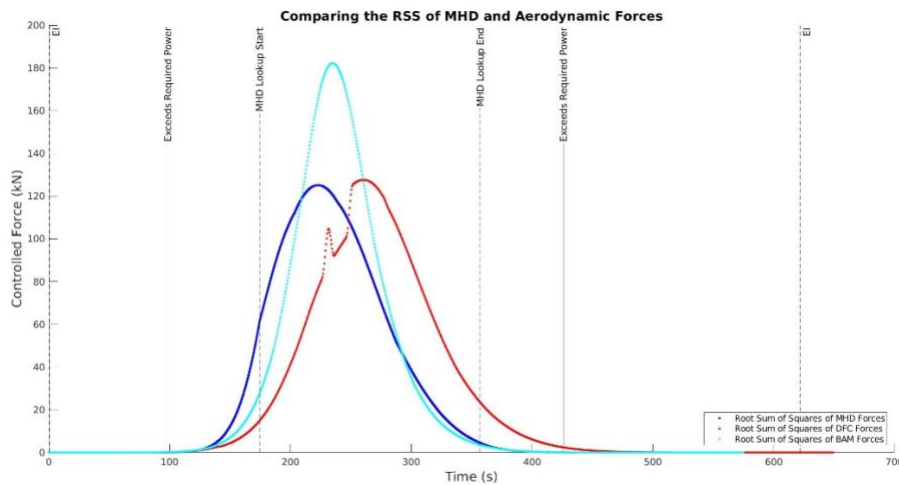
Fig. 11 Root Sum of Squares of the Forces Experienced in each Control Method.

Finally, given the shallower atmospheric pass, MHD control should expect a smaller heat flux and heat load. These results are quantified against its atmospheric counterpart in Figure (12) below. As shown, the heat flux for MHD-controlled aerocapture peaks considerably lower than the heat fluxes for the direct force control and bank angle modulation cases. After integrating each plot, the total heat loads are listed as roughly 4.8 million, 4.7 million, and 984 thousand Joules per cubic centimeter for the direct force control, bank angle modulation, and magnetohydrodynamically controlled cases, respectively. Thus, the MHD-controlled case successfully reduces the heat load by roughly 80% compared to both atmospheric cases. The heat load is directly proportional to the TPS mass; therefore, these results show that magnetohydrodynamics has the unique advantage over its atmospheric counterparts because of its ability to not only retain control authority and successfully capture in a similar amount of time but also significantly reduce the required TPS mass as well.
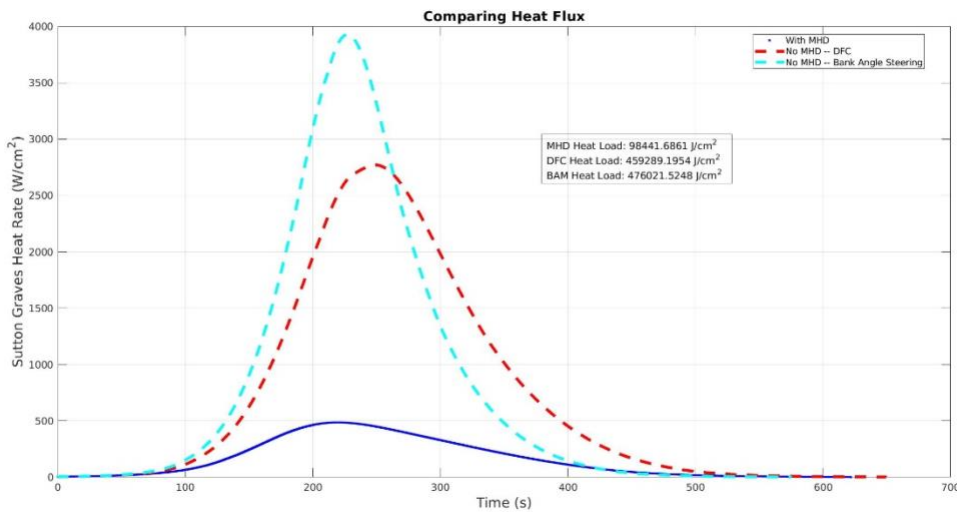

Fig. 12 Heat Fluxes and Heat Loads for each Control Method.

CONCLUSION

Throughout this research, MHD control has shown not only control authority on par with DFC and BAM but also the potential for significant TPS savings. These results verify MHD-control as a viable option and potential alternative to atmospherically controlled methods.

While magnetohydrodynamics shows promise to serve as the primary option for future larger and farther missions, it is important to note that these results are only for a nominal case tuned to a specific electromagnet configuration, and other configurations may require steeper flight path angles and thus have higher heat loads. However, for this specific point design, these savings are found to be true. Future research may refine this work in three main ways: the electromagnet design, the electrical conductivity model, the guidance algorithm, and off-nominal perturbations.

First, the electromagnet design may be further optimized to find the best combination of parameters which minimizes the mass and power while maximizing the magnetic field strength and

fusing time. Furthermore, researchers can consider electromagnetic configurations where the electromagnets are not placed at the center of gravity. While this served as a reasonable simplification for this proof of concept, the electromagnetic configuration should ideally be placed closer to the ionized plasma to maximize control authority.

Next, the electrical conductivity model had to be extrapolated below the range of 10^{-6} kg/m^3 because of the complex direct simulation Monte Carlo solvers required for the rarefied flow below that density. While this extrapolation served as a good initial estimate for this research, a more precise model would refine these results even further.

Similarly, although an open-loop guidance algorithm suffices for a proof of concept, active closed-loop guidance is ideal in actual aerocapture applications. Thus, future research should aim to apply some numerical predictor-corrector algorithm to actively change the MHD pitch angle or even the magnetic field vector magnitude to optimize the targeting solution.

Finally, while this nominal case succeeds in displaying the capabilities and potential advantages of magnetohydrodynamics, the spacecraft's initial conditions and the planet's atmosphere are dependent on numerous factors and subject to a bit of randomness the nominal model cannot encompass. Therefore, off-nominal Monte Carlo case studies perturbing the spacecraft's initial conditions and aerodynamic model as well as the planet's atmospheric model would suggest these results and advantages are true in all conditions.

NOTATION

B_x x-component of the magnetic field vector

B_z z-component of the magnetic field vector

B_0 magnetic field vector

Φ magnetohydrodynamic pitch angle

σ electrical conductivity

u_1 pre-shock atmospheric velocity

u_2 post-shock local velocity

I electromagnetic current

m	electromagnet mass
A_w	wire cross-sectional area
l_w	wire length
ρ_w	wire mass density
N	number of turns in the electromagnet
P	electromagnet power
μ_w	permeability of vacuum
σ_w	wire electrical conductivity
t_{fuse}	electrical fusing time
T_{melt}	material melting temperature in Celsius
T_{init}	material initial temperature in Celsius
n_e	electron number density
n	gas number density
T_e	electron temperature
μ_i	ion mobility
μ_e	electron mobility
n_n	neutral species number density
m_i	ion particle mass
T_2	post-shock atmospheric temperature
n_i	ion number density
$ln(\Lambda)$	Coulomb's logarithm
$\tilde{\sigma}$	ion-slip corrected electrical conductivity
F_x	x-component of the Lorentz force vector
F_z	z-component of the Lorentz force vector
K	load factor
A_{patch}	magnetohydrodynamic patch area

REFERENCES

[1] T. R. Spilker, M. Adler, N. Arora, P. M. Beauchamp, J. A. Cutts, M. M. Munk, R. W. Powell, R. D. Braun, and P. F. Wercinski, "Qualitative Assessment of Aerocapture and Applications to Future Missions," *Journal of Spacecraft and Rockets*, Vol. 56, No. 2, 2019, pp. 536–545.

[2] M. K. Lockwood, K. T. Edquist, B. R. Starr, B. R. Hollis, G. A. Hrinda, R. W. Bailey, J. L. Hall, T. R. Spilker, M. A. Noca, and N. O. O'Kongo, "Aerocapture Systems Analysis for a Neptune Mission," *NASA TM-2006-214300*, 2006.

[3] M. K. Lockwood, "Neptune Aerocapture Systems Analysis," *AIAA Atmospheric Flight Mechanics Conference and Exhibit*, 2004.

[4] M. K. Lockwood, E. M. Queen, D. W. Way, R. W. Powell, K. Edquist, B. W. Starr, B. R. Hollis, E. V. Zoby, G. A. Hrinda, and R. W. Bailey, "Aerocapture Systems Analysis for a Titan Mission," *NASA TM2006-214273*, 2006.

[5] M. K. Lockwood, B. R. Starr, J. W. Paulson, D. A. Kontinos, Y. K. Chen, B. Laub, J. Olejniczak, M. J. Wright, N. Takashima, and C. G. Justus, "Systems Analysis for a Venus Aerocapture Mission," *NASA TM-2006-214291*, March 2006.

[6] J. L. Hall, M. A. Noca, and R. W. Bailey, "Cost-Benefit Analysis of the Aerocapture Mission Set," *Journal of Spacecraft and Rockets*, Vol. 42, No. 2, 2005, pp. 309–320.

[7] S. J. Saikia, J. Millane, Y. Lu, A. Mudek, A. Arora, P. Witsberge, K. Hughes, J. M. Longuski, T. Spilker, A. Petropoulos, N. Arora, J. Cutts, J. Elliott, J. Sims, and K. Reh, "Aerocapture assessment for NASA Ice Giants Pre-Decadal Survey Mission Study," *Journal of Spacecraft and Rockets*, vol. 58, no. 2, pp. 505–515, 2021.

[8] R. G. Deshmukh, D. A. Spencer, and S. Dutta, "Investigation of Direct Force Control for aerocapture at neptune," *Acta Astronautica*, vol. 175, pp. 375–386, 2020.

[9] A. P. Girija, Y. Lu, and S. J. Saikia, "Feasibility and mass-benefit analysis of aerocapture for missions to Venus," *Journal of Spacecraft and Rockets*, vol. 57, no. 1, pp. 58–73, 2020.

[10] A. P. Girija, "Feasibility and performance analysis of Neptune Aerocapture using heritage blunt body aeroshells (pre-print)," 2020.

[11] C. L. Kelly and J. M. Little, "Performance and design scaling of magnetoshells for outer planet drag-modulated plasma aerocapture," *2021 IEEE Aerospace Conference (50100)*, 2021.

[12] Macheret, S., Shneider, M., Candler, G., Moses, R., and Kline, J., "Magnetohydrodynamic power generation for planetary entry vehicles," *35th AIAA Plasmadynamics and Lasers Conference*, 2004.

[13] Ali, H., "Magnetohydrodynamic Energy Generation and Flow Control for Planetary Entry Vehicles," *Doctoral Dissertation, Georgia Institute of Technology*, August 2019

[14] Lugo, R. A., Shidner, J. D., Powell, R. W., Marsh, S. M., Hoffman, J. A., Litton, D. K., and Schmitt, T. L., "Launch Vehicle Ascent Trajectory Simulation Using the Program to Optimize Simulated Trajectories II (POST2)." *AIAA Space Flight Mechanics Conference*, 2017.

[15] R. W. Moses, F. M. Cheatwood, C. O. Johnston, S. O. Macheret, B. Parent, J. Little, R. A. Williams, J. S. Green, M. Austin, and A. Aldrin, "New MHD lift concept for more efficient missions to Mars and Neptune," *AIAA SCITECH 2022 Forum*, 2022.

[16] M. Schoenenberger, A. Dyakonov, P. Buning, B. Scallion, and J. Van Norman, "Aerodynamic challenges for the Mars Science Laboratory entry descent and landing," *41st AIAA Thermophysics Conference*, 2009.

[17] A. Dyakonov, M. Schoenenberger, and J. Van Norman, "Hypersonic and Supersonic Static Aerodynamics of Mars Science Laboratory Entry Vehicle," *43rd AIAA Thermophysics Conference*, 2012.

[18] C. Justus, A. Duvall, and D. Johnson, "Engineering-level model atmospheres for Titan and Neptune," *39th AIAA/ASME/SAE/ASEE Joint Propulsion Conference and Exhibit*, 2003.

[19] H. L. Justh and J. Hoffman, "Neptune Global Reference Atmospheric Model (Neptune-GRAM): User Guide*", NASA TM-20205001193*, 2020.

[20] F. M. Cheatwood and P. A. Gnoffo. "User's Manual for the Langley Aerothermodynamic Upwind Relaxation Algorithm (LAURA)," *National Aeronautics and Space Administration, Langley Research Center*, 1996.

[21] J. D. Huba, "NRL: Plasma Formulary," 2004.

[17] P. Lu, C. J. Cerimele, M. A. Tigges, and D. A. Matz, "Optimal aerocapture guidance," *AIAA Guidance, Navigation, and Control Conference*, 2015.

[18] K. D. Webb, P. Lu, and A. M. Dwyer Cianciolo, "Aerocapture guidance for a human Mars Mission," *AIAA Guidance, Navigation, and Control Conference*, 2017.